ARTICLE

Tin Disulfide—An Emerging Layered Metal Dichalcogenide Semiconductor: Materials Properties and Device Characteristics

Yuan Huang,[†] Eli Sutter,[†] Jerzy T. Sadowski,[†] Mircea Cotlet,[†] Oliver L.A. Monti,[‡] David A. Racke,[‡] Mahesh R. Neupane,[§] Darshana Wickramaratne,[§] Roger K. Lake,[§] Bruce A. Parkinson,[⊥] and Peter Sutter[*,†]

[†]Center for Functional Nanomaterials, Brookhaven National Laboratory, Upton, New York 11973, United States, [‡]Department of Chemistry and Biochemistry, The University of Arizona, Tucson, Arizona 85721, United States, [§]Laboratory for Terahertz and Terascale Electronics, Department of Electrical and Computer Engineering, University of California, Riverside, California 92521, United States, and [⊥]School of Energy Resources and Department of Chemistry, University of Wyoming, Laramie, Wyoming 82071, United States

ABSTRACT Layered metal dichalcogenides have attracted significant interest as a family of single- and few-layer materials that show new physics and are of interest for device applications. Here, we report a comprehensive characterization of the properties of tin disulfide (SnS_2), an emerging semiconducting metal dichalcogenide, down to the monolayer limit. Using flakes exfoliated from layered bulk crystals, we establish the characteristics of single- and few-layer SnS_2 in optical and atomic force microscopy, Raman spectroscopy and transmission electron microscopy. Band structure measurements in conjunction with *ab initio* calculations and photoluminescence spectroscopy show that SnS_2 is an indirect bandgap semiconductor over the entire thickness range from bulk to single-layer. Field effect transport in SnS_2 supported by SiO_2/Si suggests predominant scattering by centers at the support interface. Ultrathin transistors show on—off current ratios $>10^6$, as well as carrier mobilities up to 230 cm^2/(V s), minimal hysteresis, and near-ideal subthreshold swing for devices screened by a high-*k* (deionized water) top gate. SnS_2 transistors are efficient photodetectors but, similar to other metal dichalcogenides, show a relatively slow response to pulsed irradiation, likely due to adsorbate-induced long-lived extrinsic trap states.

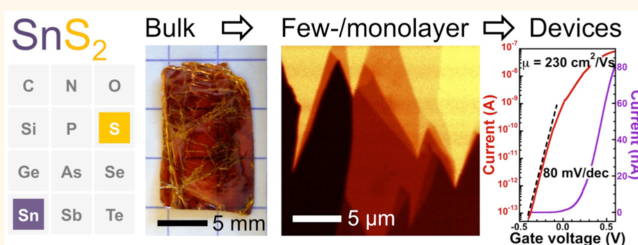

KEYWORDS: tin disulfide · 2D materials · monolayer · field-effect transistor · photodetector · charge transport

Two-dimensional materials, such as graphene and hexagonal boron nitride, have attracted considerable interest since their first isolation by mechanical exfoliation from layered bulk crystals.[1] Graphene has provided access to new physics at reduced dimensionality[2−5] and has demonstrated extreme mechanical,[6] optical,[7] and sensing properties;[8] boron nitride is finding applications as an ideal electrically insulating complement to graphene for in-plane[9−11] and vertical heterostructures.[12] Fundamentally and technologically interesting properties have been identified in layered metal dichalcogenides (LMDs) in the ultrathin limit, with most attention to date focused on semiconducting transition metal dichalcogenides, particularly MoS_2.[13] MoS_2 monolayers (*i.e.*, a single, covalently bonded S—Mo—S trilayer) and related materials have shown relatively high charge carrier mobility (>200 cm^2/(V s)) combined with high on—off current ratios in field-effect transistors,[14] sensitive photodetectors,[15,16] and exceptionally high optical absorption in photovoltaic devices.[17,18] The electronic bands of MoS_2 derive from combinations of molybdenum d- and sulfur p-orbitals, whose different sensitivity to interlayer coupling along with confinement effects is responsible for an indirect-to-direct bandgap transition from bulk/few-layer to monolayer MoS_2.[19−22] High atomic number metals or transition metals give rise to strong spin—orbit interactions that can induce large valence band splitting.[19−21] Energetically degenerate conduction band valleys at different momentum give rise to new quantum numbers, and the coupling of

* Address correspondence to psutter@bnl.gov.

Received for review August 11, 2014 and accepted September 23, 2014.

Published online September 23, 2014
10.1021/nn504481r

© 2014 American Chemical Society

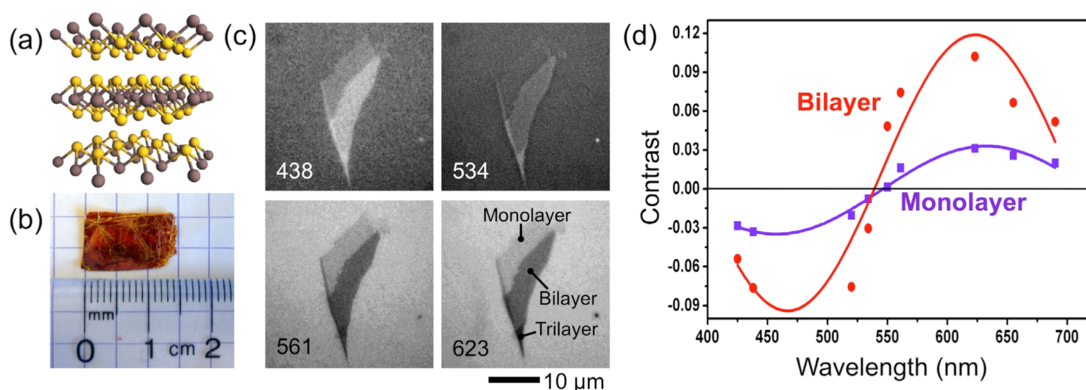

Figure 1. From bulk to monolayer SnS_2. (a) Crystal structure of layered bulk SnS_2. (b) SnS_2 single crystal grown by the Bridgman method. (c) Optical bright field microscopy image of a SnS_2 flake with partial monolayer, bilayer, and trilayer thickness (as confirmed by AFM, see Figure 2), supported by 300 nm SiO_2/Si. Representative images obtained at different illumination wavelength (as given, in nm), showing the evolution of optical contrast of the substrate, monolayer, and bilayer SnS_2. (d) Measurements of the optical contrast of monolayer and bilayer SnS_2 on 300 nm SiO_2/Si at different wavelengths. Lines are guides to the eye.

spin and valley degrees of freedom are being investigated for novel approaches to information processing.[23,24] Finally, recent progress in bottom-up synthesis promises access to high-quality, large-area materials for future device applications.[25]

While MoS_2 has become a prototype LMD, other materials may show new physics or have properties optimized for particular applications. The surprising and rich new physics emerging in the low-dimensional limit suggests strongly that other van der Waals layered materials may exhibit novel behavior. Moreover, for widespread use in devices, the discovery of earth-abundant two-dimensional and layered materials is essential. Tin disulfide (SnS_2) is a semiconducting LMD comprising earth-abundant constituents, notably a group IV element (Sn) replacing the transition metal in MoS_2 and related compounds. Bulk SnS_2 crystals have long been investigated for photovoltaics[26] and photoelectrochemistry,[27] and early efforts have already shown some progress in using van der Waals epitaxy for the controlled bottom-up synthesis of SnS_2 films,[28] as well as nanoscale etching by scanning probe methods.[29,30]

Recently, first reports have emerged on the isolation of high-quality few-layer and monolayer SnS_2 by chemical[31] and mechanical exfoliation[32−34] from layered crystals, as well as their use as a photocatalyst for visible light water splitting,[31] in field-effect devices,[33,34] and in simple logic circuits.[32] However, at this point it remains unclear if monolayer SnS_2 has indeed been obtained, primarily because in contrast to the more established LMDs, notably MoS_2, the characterization of few-layer SnS_2 is still poorly developed and basic properties of this material are not well understood. Examples are the unambiguous identification of monolayer SnS_2, as well as thickness measurements on few-layer SnS_2 using scanning probe microscopy, Raman spectroscopy, and optical microscopy; the development of the electronic band structure with reduction in thickness (*i.e.*, the possibility of a transition to a direct bandgap in the monolayer, similar to MoS_2); transport properties in field-effect transistors, especially the factors limiting the achievable carrier mobility; and the possibility of using SnS_2 for light detection applications. Here, we comprehensively characterize high-quality bulk SnS_2 crystals as well as ultrathin exfoliated flakes to establish unambiguously and for the first time the fundamental properties of SnS_2 in bulk, few-layer, and monolayer form and thus create the basis for the systematic exploration of this material in research and in potential applications including nanoelectronics, optoelectronics, as well as light harvesting and other energy conversion applications.

RESULTS AND DISCUSSION

Figure 1 illustrates experiments on the isolation of monolayer and bilayer SnS_2 from layered bulk crystals, as well as their identification by optical microscopy. SnS_2 crystallizes in a CdI_2-type layered structure, in which S−Sn−S trilayers with internal covalent bonding are held together by van der Waals forces (Figure 1 (a)). SnS_2 occurs in different polytypes with the same structure of the S−Sn−S layers but different interlayer stacking.[35,36] While the exact conditions giving rise to the different polytypes remain unclear, previous reports suggested that low-temperature synthesis produces the 2H-polytype, while crystal growth at temperatures above 800 °C tends to give 4H-SnS_2 (Figure 1 (a)).[37,38]

Mechanical exfoliation from large layered bulk crystals grown by the vertical Bridgman method (Figure 1 (b)) can be used to obtain flakes with varying thickness, which often contain monolayer or bilayer areas with lateral dimensions exceeding 10 μm. These thin sections are easily identified *via* their optical contrast on 300 nm SiO_2/Si substrates, similar to other 2D and

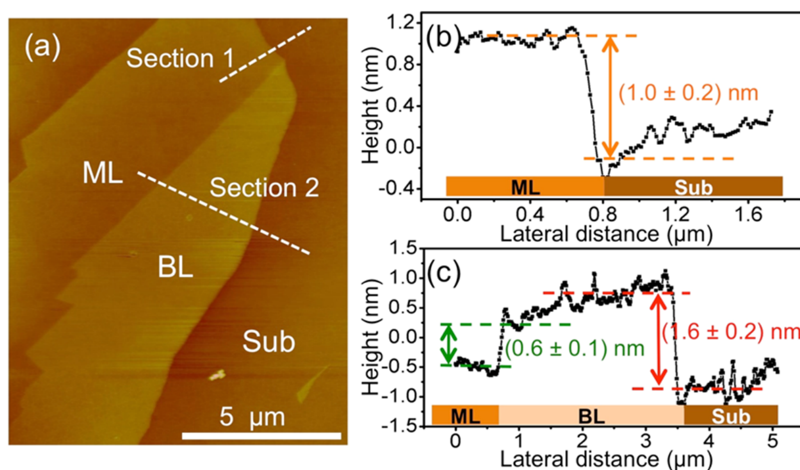

Figure 2. Atomic force microscopy of monolayer and bilayer SnS_2 on SiO_2. (a) AFM image of a flake of monolayer and bilayer SnS_2 (same as shown in Figure 1). (b,c) Height profile of sections 1 and 2 in (a). The thickness of monolayer (ML) SnS_2 is about 1 nm above the SiO_2 support (b); the thickness of the bilayer (BL) is about 1.6 nm above the SiO_2 surface, whereas the step between monolayer and bilayer SnS_2 is 0.6 nm. The observed thicknesses are similar to those of monolayer and bilayer MoS_2.[42]

layered materials.[39−41] While the areas with weakest optical contrast can be difficult to find in bright-field microscopy with white light illumination, color-filtered bright-field as well as dark-field images clearly show these thinnest flakes. We have used optical microscopy (Figure 1 (c,d)) combined with atomic force microscopy (AFM, Figure 2) to unambiguously demonstrate the successful isolation of monolayer and bilayer SnS_2. Microscopy with monochromatic illumination (in reflection) gives strong contrast between monolayer and bilayer SnS_2, and between thin flakes and the substrate. Figure 1 (c) shows representative micrographs, in which the optical contrast varies with wavelength. Contrast maxima between monolayer and bilayer SnS_2 are found at ~475 and ~625 nm, with a contrast minimum, *i.e.*, simultaneously invisible monolayer and bilayer SnS_2 on 300 nm SiO_2/Si, at ~550 nm illumination wavelength.

AFM imaging provides an independent measurement of the absolute thickness of flakes of 2D materials. AFM applied to the same flake shown in Figure 1 has been used to corroborate the optical thickness assignment (Figure 2). AFM images confirm that this flake consists of two larger parts with different height above the SiO_2 support (Figure 2 (a)). The height of section 1 above the SiO_2 is (1 ± 0.2 nm) (Figure 2 (b)), which is consistent with measurements for single-layer graphene and MoS_2. Even though the actual thickness of monolayer SnS_2 is ~0.6 nm, the measured value is always around 1 nm, likely due to the trapping of adsorbed molecules (*e.g.*, H_2O) between the flake and the substrate. When measuring the height profile along section 2 (Figure 2 (c)), the height change at the edge between the thinner and thicker segment of SnS_2 is 0.6 nm, while the height of the thicker section above the SiO_2 support is 1.6 nm. We conclude that the flake analyzed here indeed consists of monolayer and bilayer SnS_2. A previous report assigned a thickness of 1.8 nm measured by AFM to monolayer SnS_2/SiO_2,[34] but our results suggest that this thickness instead corresponds to bilayer SnS_2.

Raman spectroscopy has proven to be a versatile tool for studying 2D materials, such as graphene, MoS_2 and others.[43,44] We used Raman spectroscopy to identify the stacking sequence (*i.e.*, crystal polytype) of our bulk SnS_2 starting material, and to map and quantify the thickness of few-layer SnS_2. Smith *et al.* have established the Raman spectra of different polytypes of layered SnS_2.[45] Comparison with the modes observed in spectra of the bulk SnS_2 crystal used in our exfoliation experiments allows an unambiguous identification of the polytype of our material as 4H-SnS_2 (Figure 3 (a)). In the 4H polytype, the most intense Raman line at 313.5 cm^{-1} is due to a mixture of A_1 and E optical modes. This line is very close to the A_{1g} mode of 2H-SnS_2 (315 cm^{-1}),[45] and therefore does not lend itself well to fingerprinting of the polytype. Instead, the E-mode at lower energy allows a facile discrimination between 2H- and 4H-polytypes. The E_g mode of 2H-SnS_2 gives rise to a single, intense band at 205 cm^{-1}, whereas the E-mode of 4H-SnS_2 gives rise to a doublet at 200 and 214 cm^{-1}, respectively. Our measurements at two excitation wavelengths clearly show the doublet, *i.e.*, the bulk crystal used in our experiments is 4H-SnS_2.

Figure 3 (b) shows an optical image of an exfoliated SnS_2 flake, in which the number of layers varies from 2 to 8 (and further to ~20 layers outside the field of view shown in Figure 3 (b)), supported by 300 nm SiO_2/Si. For few-layer 4H-SnS_2, we track Raman scattering from the most intense (A_1+E) optical phonon mode; the most prominent band originating in the SiO_2/Si support, the zone-center optical phonon of Si at ~520 cm^{-1} serves as a reference. A comparison of the optical micrograph with a Raman map of the (A_1+E) phonon (280−320 cm^{-1}, Figure 3 (c)) shows that the

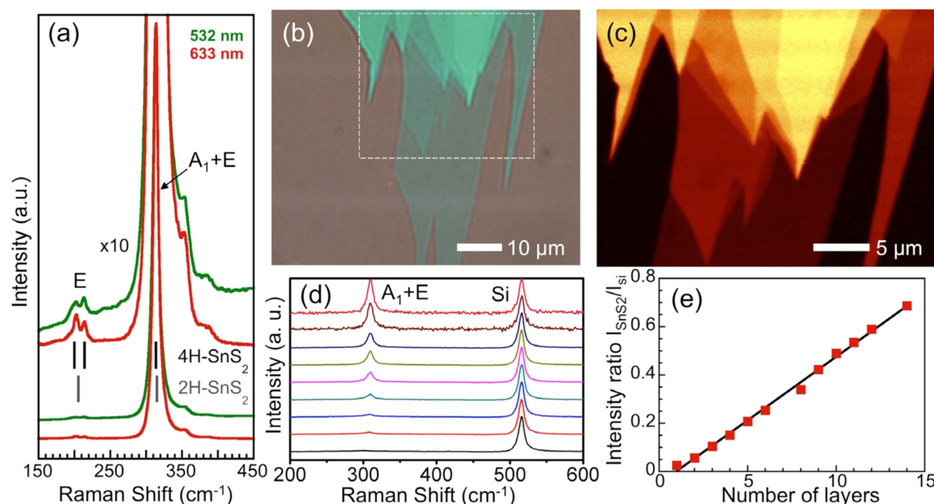

Figure 3. Raman spectroscopy and measurement of the thickness of SnS_2. (a) Raman spectra of bulk SnS_2 at two excitation wavelengths (532 nm, 633 nm). Gray and black vertical lines mark the main Raman lines of 2H- and 4H-SnS_2 as identified by Smith *et al.*[45] (b) Optical microscopy image of a SnS_2 flake with several areas of different thickness. (c) Raman intensity map (280—320 cm^{-1}) of the area outlined in (b), showing the intensity of the (A_1+E) mode in areas of different thickness within the flake. Thicker SnS_2 gives rise to higher intensity. (d) Normalized Raman spectra of SnS_2 from monolayer to multilayer. The intensity of the Si peak is set as constant. (e) Intensity ratio of the (A_1+E) peak of SnS_2 and of the zone center optical phonon of Si (520 cm^{-1}) as a function of the number of layers.

intensity of this band scales with the thickness of the SnS_2. The signal intensity within each terrace (*i.e.*, at constant thickness) is constant, but it abruptly increases with each added layer. To quantify the thickness dependence, we measured Raman spectra at different locations within the flake. Each spectrum was normalized to the intensity of the Si peak (Figure 3 (d)). A transition of the (A_1+E) mode of few-layer 4H-SnS_2 into the A_{1g} phonon occurs for monolayer and bilayer SnS_2, whose thickness is below that of the unit cell of the 4H-polytype. The A_{1g} mode shows low intensity but is still detectable and can be clearly distinguished for monolayer and bilayer SnS_2. A plot of the intensity ratio of I(SnS_2) to I(Si) as a function of the number of layers is shown in Figure 3 (e). For monolayer SnS_2/SiO_2, the intensity ratio is ~0.02, and it increases to 0.96 for ~20 layer SnS_2 within the flake. Over this entire thickness range, the I(SnS_2)/I(Si) intensity ratio increases approximately linearly with thickness, and it exhibits high reproducibility in samples with the same number of layers. Hence, with a calibration as given in Figure 3 (e), Raman spectroscopy can serve as a simple and reliable method for measuring the thickness of few-layer SnS_2 across an extended thickness range.

Transmission electron microscopy (TEM) was used to assess the interlayer spacing (cross-section) and the high-resolution TEM (HR-TEM) lattice contrast (plan-view) of few-layer SnS_2 exfoliated onto holey carbon grids. Figure 4 (a) shows part of a few-layer SnS_2 flake on the holey carbon TEM grid. A folded edge of the flake makes it possible to observe the layered structure and to determine the number of atomic layers (Figure 4 (b)). From the cross-sectional image, the interlayer spacing is measured to (0.62 ± 0.015) nm (Figure 4 (c)), in excellent agreement with the AFM results. HR-TEM images along the [001] zone axis (perpendicular to the flake) show a hexagonal lattice with a nearest-neighbor spacing of 0.32 nm, and with a slight modulation of the intensity of the lattice fringes (Figure 4 (d)). Multislice TEM image simulations[46] for 4H-SnS_2 closely reproduce this image contrast (Figure 4 (e)), and show that the intensity maxima correspond to two types of atomic columns: the brighter maxima are due to mixed columns of Sn and S atoms, arranged in a honeycomb-like formation; the slightly darker maxima originate from columns that are populated only by S atoms (Figure 4 (f)). Transmission electron diffraction, finally, shows a pattern that can be unambiguously indexed to 4H-SnS_2 along the [001] zone axis (Figure 4 (g)).

One of the unique aspects of metal dichalcogenide materials, such as MoS_2 or SnS_2, is the fact that their electronic bands have mixed character with different contributions from metal d-orbitals and p-orbitals of the chalcogen species. In MoS_2, the different character of valence and conduction bands at different locations in the Brillouin zone (BZ) implies different sensitivity to interlayer coupling and confinement, with S p-orbital derived states being more sensitive to these factors than bands with predominant contribution from Mo d-orbitals, localized at the center of the S−Mo−S trilayer. As a result, significant shifts in the band edges give rise to a transition from an indirect to a direct bandgap as the thickness of MoS_2 is reduced from bulk/few-layer to a single monolayer.[19,20] We have previously observed this transition *via* micro-ARPES band mapping on μm sized exfoliated MoS_2.[21] Here, we use a similar approach to measure the electronic band structure of bulk-like SnS_2. The experimental

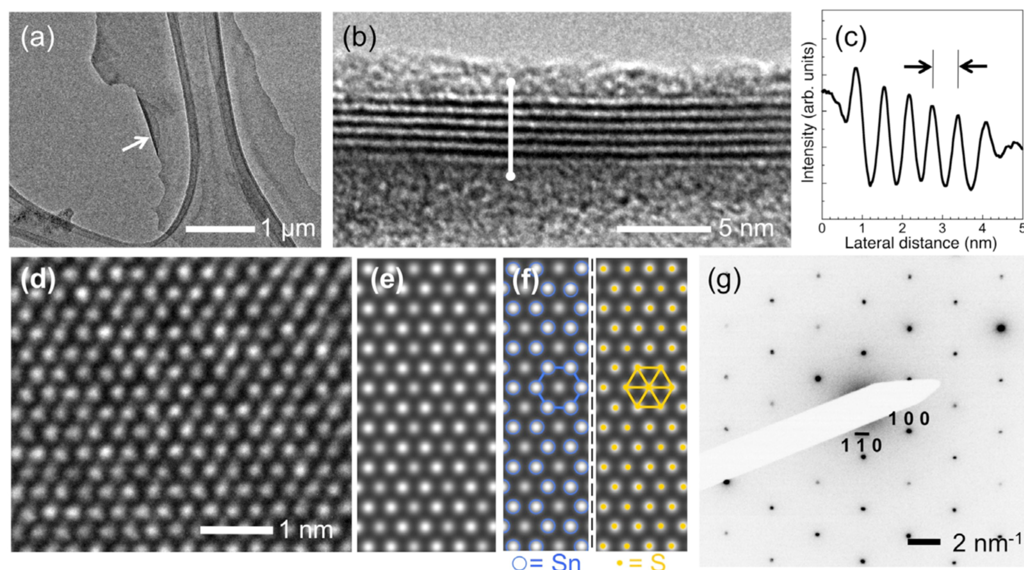

Figure 4. TEM imaging of few-layer SnS_2. (a) Low-magnification image of a SnS_2 flake on holey carbon grid. Arrow: Folded edge of the flake. (b) Cross-sectional TEM along the folded edge of the SnS_2 flake, showing the layered structure with 6 atomic layers. (c) Intensity profile along the line marked in (b). The measured layer distance is 0.62 nm. (d) Plan-view high-resolution TEM of the SnS_2 lattice structure. (e) Multislice image simulation for the 4H-polytype of SnS_2. (f) Simulated HR TEM image showing the positions of Sn and S atoms in the 4H-SnS_2. (g) Electron diffraction pattern obtained along [001] zone axis.

band map is then used to validate calculated band structures of bulk SnS_2, and calculations of the electronic structure of bulk and monolayer SnS_2, combined with photoluminescence measurements, are used to explore if this material shows an indirect-to-direct bandgap transition similar to MoS_2.

Mirror-mode LEEM images of freshly cleaved SnS_2 crystals show large, flat terraces with lateral dimensions up to several tens of micrometers. The LEED patterns obtained from cleaved crystals exhibit sharp spots with hexagonal symmetry, as expected for the basal plane of SnS_2,[38] without annealing of the sample. A LEED pattern obtained at E = 28 eV (Figure 5 (a)) shows two sets of first-order diffraction spots with alternating high and low intensity, consistent with SnS_2 with the interlayer stacking of the 4H-polytype. Across large distances on the surface (several tens of μm), the stacking sequence varies occasionally (*i.e.*, there are stacking faults), as shown by complementary LEED patterns in which the two sets of spots are interchanged.

The electronic band structure of SnS_2 has been investigated in several computational studies dating back to the 1970s.[47−49] Progressively more accurate methods were used,[50] and more recently calculations including corrections for van der Waals forces have been carried out.[51] Early photoemission experiments have provided energy distribution curves for SnS_2,[52,53] but to date no high-quality maps of the band dispersion have been available to validate the band structure calculations. We obtained micro-ARPES band structure maps at room temperature with an energy resolution better than 300 meV, using energy-filtered photoelectron angular distributions mapped in reciprocal space by the electron optics and detector system in spectroscopic LEEM.[21,54] The raw data consist of sets of photoelectron angular distribution maps in reciprocal space, obtained with an energy step of 0.1 eV. Projections along high-symmetry directions in the Brillouin zone were used to generate band dispersion maps, as shown in Figure 5 (b).

To gain further insight, we computed the bandstructure of bulk 4H-SnS_2 and monolayer SnS_2 using *ab initio* density-functional theory (DFT). The optimized lattice constants for 4H-SnS_2 are a = 0.37 nm and c = 1.3328 nm, consistent with the structural parameters measured in TEM. An overlay of the calculated bands on the experimentally determined bulk band structure shows excellent agreement. The calculations give a fundamental bandgap of bulk 4H-SnS_2 E_g = 2.308 eV, somewhat larger than the gap determined experimentally by optical absorption measurements on thicker SnS_2 flakes (Figure S1), and observed in photoluminescence (PL) spectra (Figure S2). The gap is indirect, with the valence band maxima (VBM) located along the $\Gamma-M$ high-symmetry direction and the conduction band minima (CBM) at the M valley of the BZ. The fundamental bandgap of monolayer SnS_2 is 2.033 eV and remains indirect, with the valence band maxima located along $\Gamma-M$, and the conduction band minima at the M valley. This behavior is in contrast to MoS_2, which shows an enhancement of the PL intensity due to a transition from an indirect (bulk, few layer MoS_2) to a direct gap (monolayer MoS_2). The transition to a direct gap in MoS_2 results from a significant shift of the valence band edge at Γ. Whereas the valence band maximum lies at Γ for thicker MoS_2, its hybrid of antibonding

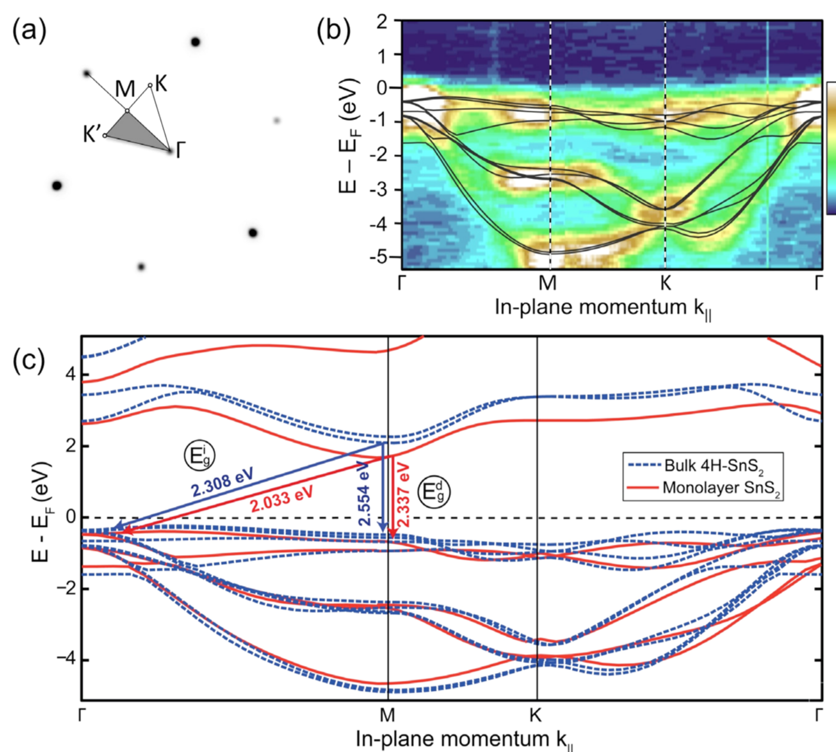

Figure 5. Surface structure and electronic band structure of SnS_2. (a) Low-energy electron diffraction pattern with overlaid irreducible wedge of the surface Brillouin zone. (b) Angle-resolved photoelectron spectroscopy of the projected band structure of bulk SnS_2. False color scale: Dark blue, lowest intensity; white, highest intensity. Black lines are results of our DFT band structure calculations for 4H-SnS_2 using the HSE hybrid functional. (c) Comparison of the calculated band structure of bulk (4H) and monolayer SnS_2. In the transition from bulk to monolayer SnS_2 the energy of the valence band maximum (along ($\Gamma-$M)) remains approximately the same. The conduction band minimum at M for the monolayer structure undergoes a downward shift of 245 meV compared to the bulk. The energy shifts are obtained relative to the vacuum level. The fundamental bandgap (between M and Γ) is only weakly affected and remains indirect in the transition from bulk to monolayer SnS_2.

sulfur p_z orbitals and Mo $d_z{}^2$-states experiences a significant downward shift with the elimination of interlayer coupling in the transition to monolayer thickness. This shifts the valence band states at Γ to a lower energy than the valence band edge at K, and thus a direct gap forms at K. In comparison, our calculations show the bandgap of SnS_2 to be quite insensitive to the thickness, down to a single monolayer. This different behavior can be explained by the orbital composition of the conduction and valence band edges. In both bulk and monolayer SnS_2, the valence band edge along $\Gamma-$M is dominated ($\sim$90%) by sulfur p_x and p_y (*i.e.*, in-plane) orbitals. The conduction band edge at the M valley is a hybrid of 51% tin s-orbitals and 37% sulfur p_x and p_y orbitals and 8% sulfur p_z orbitals. Whereas some of the higher-lying bands with sulfur p_z character show substantial shifts, these are not sufficiently large to affect the fundamental (indirect) bandgap, which involves states that are insensitive to both interlayer coupling and confinement.

To experimentally confirm the absence of an indirect-to-direct bandgap transition from few-layer to monolayer SnS_2, we performed measurements of the integrated photoluminescence (PL) intensity from SnS_2 flakes of different thickness. Figure S3 shows an analysis of PL intensity measurements on few-layer and monolayer SnS_2. To minimize substrate contributions to the PL, the flakes have been supported on sapphire. PL maps generally show higher intensity for thicker SnS_2 layers. This trend is confirmed by an analysis of the PL intensity from areas of different thickness: the measured PL decreases linearly from 5 layers to 1 layer thickness, and extrapolates to the PL of the bare substrate. Hence, monolayer SnS_2 does not exhibit enhanced PL compared to few-layer material, which further supports our theoretical result that SnS_2 remains an indirect bandgap semiconductor across the entire thickness range from bulk to single layer.

Aside from the new physical phenomena found in metal dichalcogenides, the semiconducting members of this larger family of layered/monolayer systems have attracted particular interest for electronic and optoelectronic applications.[14,55] Intrinsic bandgaps in the range of 1 to 3 eV make these materials suitable for use in photodetectors and photovoltaic devices, and they may be advantageous over the semimetallic graphene for certain applications, *e.g.*, in flexible electronics or digital logic. To determine the electronic transport properties of few-layer SnS_2 and the potential of this LMD for applications in electronics and optoelectronics,

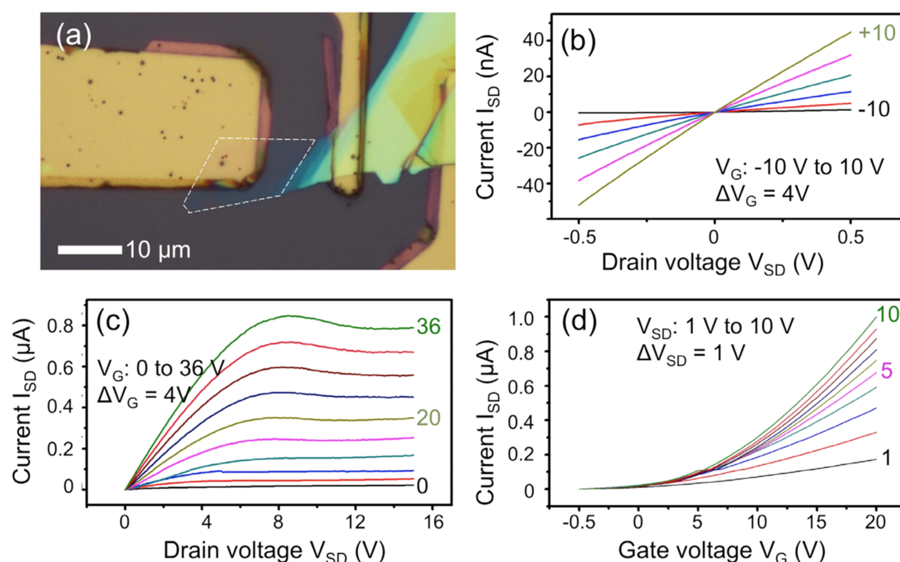

Figure 6. Electrical transport in SnS_2 FET devices. (a) Optical image of one SnS_2 device. The outline marks the SnS_2 channel (3 monolayers thick). (b) $I_{SD}-V_{SD}$ curves at low bias, for gate voltage ranging from −10 to 10 V; the linearity of $I_{DS}-V_{DS}$ indicates an excellent ohmic contact in the device. (c) $I_{SD}-V_{SD}$ curves at higher bias, V_{SD}, for gate voltages ranging from 0 to 36 V. (d) Relationship between I_{SD} and V_G for V_{SD} ranging from 1 to 10 V.

we fabricated field-effect transistors (FETs) from exfoliated SnS_2 flakes (Figure 6 (a)). The device characteristics of these FETs were then measured at room temperature.

Figure 6 (b−d) summarize the measurements on a representative device, which was back-gated *via* the 300 nm SiO_2/Si of the support. At low source-drain voltage, the current−voltage characteristics (I_{SD} *vs* V_{SD}) are symmetric and linear over the entire range of gate voltages from −10 V to +10 V, which indicates ideal ohmic contacts between the Ti/Au electrodes and the SnS_2 channel. With back-gate voltage V_G applied to the Si substrate, I_{SD} gradually increases as the gate voltage is changed from −10 to 10 V, as shown in Figure 6 (b). Figure 6 (c) shows $I_{SD}-V_{SD}$ characteristics in a larger range of V_{SD} from 0 to 15 V, with back-gate voltage changing from 0 to 36 V in steps of 4 V. I_{SD} is linear at low V_{SD} and saturates at higher bias. As V_G varies from 0 to 36 V, I_{SD} changes from 1.8×10^{-13} A to 8.5×10^{-7} A, corresponding to an on−off current ratio of $\sim 4.7 \times 10^6$. The device shows excellent n-type transistor behavior as can be seen in Figure 6 (d). The field-effect mobility has been calculated using the following equation:

$$\mu = \frac{dI_{SD}}{dV_G} \cdot \frac{L}{WC(SiO_2)V_{SD}} \qquad (1)$$

where L and W are the length and width of the device, and $C(SiO_2) = 11.6$ nF/cm^2 is the capacitance of the 300 nm SiO_2 layer.[56] On the basis of the data shown in Figure 6, we determine a room temperature mobility of 5 cm^2/(V s). The mobility of this device is larger than previously reported for few-layer SnS_2 FETs (~1 cm^2/(V s)),[32] but about 1 order of magnitude lower than in a top-gated SnS_2 device using a Al_2O_3 dielectric layer.[34]

Results on MoS_2 FETs have suggested that the mobility of monolayer and few-layer metal dichalcogenides supported on SiO_2 is primarily limited due to scattering by charged impurities in the oxide.[14] To test if charged impurity scattering is limiting the field-effect mobility in few-layer SnS_2 FETs, we fabricated a series of devices with different thickness of the SnS_2 channel. Given that an increasing fraction of the charge carriers are removed successively further away from any interfacial scattering centers, the measured "effective" carrier mobility should increase as the channel becomes thicker if interfacial impurity scattering is the primary mobility-limiting scattering mechanism. The results of transport measurements on SnS_2 FETs with different channel thickness, determined for each of these devices by AFM, are summarized in Figure 7 (a).

The effective field-effect carrier mobility in this batch of identically processed devices indeed shows a continuous increase with increasing thickness of the SnS_2 channel, from ~1.5 cm^2/(V s) (10 nm thick) to ~20 cm^2/(V s) (120 nm thick). In a simple model, we can consider the device channel as a system of discrete parallel conductors with different carrier densities n_j (decreasing with growing separation from the SiO_2 interface due to reduced gate-coupling) and different mobilities μ_j. The conductivity of the entire system is given by

$$\sigma = \sum_j q n_j \mu_j = q n_{eff} \mu_{eff} \qquad (2)$$

where n_{eff} and μ_{eff} denote "effective" carrier densities and mobilities of the device overall. In a device with a large channel thickness, one would expect that the carriers near the top of the channel, which are screened from the charged impurity scattering centers in the

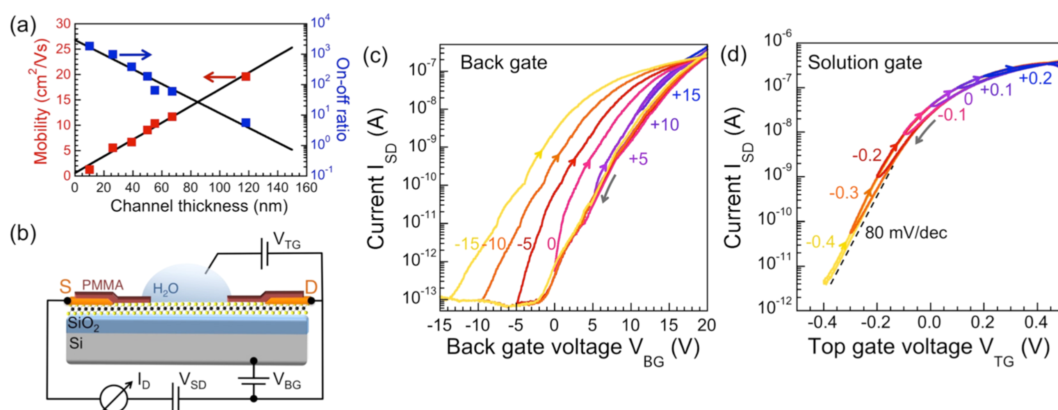

Figure 7. Mobility-limiting scattering in few-layer SnS_2 FETs and its screening in top-gated devices. (a) Field-effect mobility in SnS_2 FETs as a function of the channel thickness. Error bars, AFM measurements of the channel thickness: ± 3 nm for thickness >30 nm; mobility: ± 0.5 cm^2/(V s) for μ > 5 cm^2/(V s). (b) Schematic diagram of the geometry of SnS_2 FET devices with SiO_2/Si back gate and H_2O solution top gate. For an optical micrograph of an actual device, see Figure S8. (c) Transfer characteristics (I_{SD} *vs* V_{BG}) of a back-gated SnS_2 device (~8 layers), measured with dual back gate sweeps starting at +20 V, with turnaround points between +15 V and −15 V. The transfer characteristics show significant hysteresis. (d) Analogous transfer characteristics (I_{SD} *vs* V_{TG}) of a deionized (DI) water top-gated SnS_2 device, measured with dual top gate voltage sweeps, starting at +0.5 V, with turnaround points between +0.2 V and −0.4 V. The device shows minimal hysteresis and a near-ideal subthreshold swing of 80 mV/decade.

SiO_2 by the intervening SnS_2, would have a mobility that significantly exceeds the measured effective value, μ_{eff}. This expectation is confirmed by further considering eq 2. Given that the permittivity of metal dichalcogenides is nearly the same as that of SiO_2 ($\varepsilon \sim 4\ \varepsilon_0$), the induced carrier density $n(z)$ in the SnS_2 at distance z from the interface of the SiO_2 gate dielectric (thickness d_{ox}, here 300 nm) scales as $n(z) \propto (\varepsilon)/(d_{ox} + z)$.[57] The effective (*i.e.*, measured) mobility of a FET with a thick channel then becomes a weighted sum of the mobilities of the carriers in the individual parallel conductors:

$$\mu_{eff} = \frac{\sum_i (d_{ox}+z_i)^{-1}\mu_i}{\sum_i (d_{ox}+z_i)^{-1}} \qquad (3)$$

As an example, if scattering at the SnS_2/SiO_2 interface limits the carrier mobility, an overall, effective mobility μ_{eff} = 20 cm^2/(V s) at 120 nm SnS_2 channel thickness (Figure 7 (a)) implies that the charge carriers near the top of the channel have a mobility of ~45 cm^2/(V s). This estimate suggests an actual limit due to scattering centers intrinsic to the channel material, such as defects, dopants or other impurities in the SnS_2, beyond ~50 cm^2/(V s).

Clearly, increasing the channel thickness is not a suitable approach for enhancing the properties of practical transistors made from layered materials. This is illustrated for our SnS_2 devices by plotting the on−off current ratio as a function of channel thickness (Figure 7 (a)). While the effective carrier mobility can be increased in thicker device channels, gate control over the current flow in the channel becomes at the same time progressively compromised. Even for the smallest channel thickness shown in Figure 7 (a) (10 nm), the on−off ratio (~2 × 10^3) is substantially lower than for ultrathin devices consisting of only 1−3 layers of SnS_2 (~5 × 10^6, Figure 6). Increasing the channel thickness beyond 10 nm causes a further exponential loss in gate control, *i.e.*, the transistor can no longer be turned off efficiently by the back gate.

Experiments on monolayer MoS_2 transistors have shown that top gating by a high-*k* dielectric, such as HfO_2, can effectively screen scattering centers in the SiO_2 support while maintaining very high on−off current ratios.[14] To explore this effect for SnS_2 FETs, we fabricated devices that in addition to back gating could be gated using a liquid top-gate with deionized (DI) water ($\varepsilon \sim 80\ \varepsilon_0$) as the dielectric. Solution gating has been widely used recently, primarily because it is a simple way for achieving very high carrier densities by field-effect doping of different materials, such as MoS_2,[58] graphene,[59] and several superconductors.[60,61] After fabricating conventional (back gated) SnS_2 FET devices as described above, we provided an additional patterned insulating layer by spin-coating PMMA and opening windows for access of the liquid to the FET channel, as shown schematically in Figure 7 (b) (see also Figure S8). We first measured the electrical properties of this device without DI water (*i.e.*, as a back-gated FET), as shown in Figure 7 (c) (Figure S7 (a,b)). The characteristics are similar to those of our conventional back-gated devices (*e.g.*, Figure 6). Again, the drain current increases gradually as the gate voltage (V_{BG}) is changed from 0 to 20 V, *i.e.*, the back-gate provided control over the conductance of the FET. The field-effect mobility of this device controlled by the back gate is ~2 cm^2/(V s). Then we deposited a drop of DI water onto this device and applied the gate bias (V_{TG}) between this solution top gate and the source

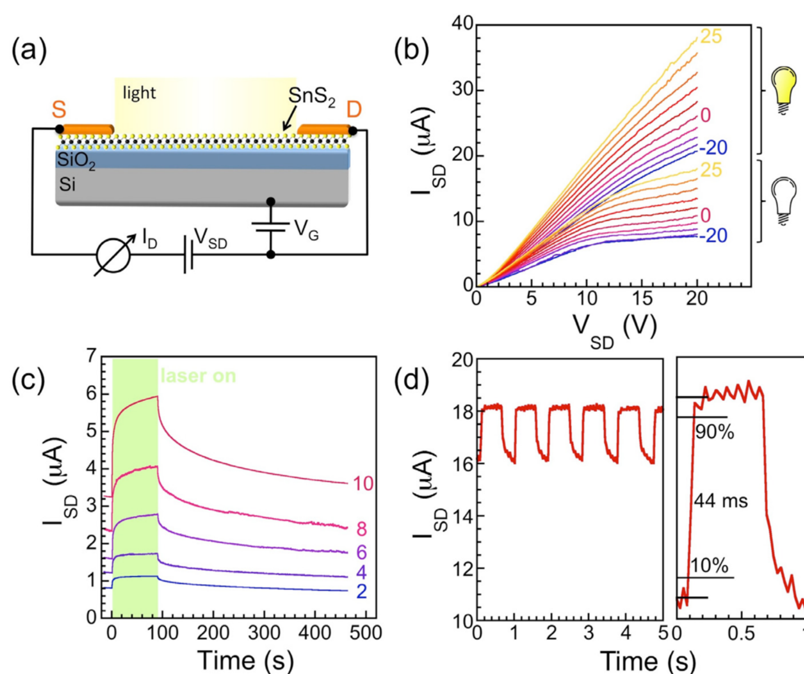

Figure 8. Light detection *via* photoconductivity in SnS_2 FETs. (a) Schematic of the SnS_2 photo-FET. S: source; D: drain electrode. (b) $I_{SD}-V_{SD}$ curves at low bias for back-gate voltages between −20 V and +25 V (in 5 V steps), without and with illumination. Light source: halogen lamp. (c) Detection of pulsed illumination at gate voltages from +2 V to +10 V. Light source: laser diode. (d) Response under chopped laser illumination (f = 1.0 Hz) and measurement of a 10%−90% rise time of ∼44 ms.

electrode (Figure 7 (d)). The $I-V$ curves of the solution-gated FET device again show linear and symmetric behavior, indicating ohmic contacts and absence of leakage currents (Figure S7 (c,d)). I_{SD} increased to 190 nA at V_{SD} = 40 mV and at a solution gate voltage V_{FG} = 500 mV, compared to 2.5 nA at V_{SD} = 40 mV at a gate bias V_{BG} = 5 V for back-gated operation. The transfer characteristic of the solution gated FET shows a near-ideal subthreshold swing of ∼80 mV/decade (Figure 7 (d); Figure S8). To be able to determine the carrier mobility in the solution gated FET devices, we performed additional transport experiments aimed at measuring the specific double-layer capacitance of DI water in contact with the SnS_2 device channel. We find $C(H_2O)$ = 137 nF/cm^2, from which we calculate field-effect mobilities of solution-gated FETs between ∼60 cm^2/(V s) and over 200 cm^2/(V s). The highest room temperature mobility measured in SnS_2 devices in this study is 230 cm^2/(V s) (Figure S8), which significantly exceeds the highest field-effect mobility of SnS_2 devices reported to date (∼60 cm^2/(V s))[34] and is comparable to the highest mobilities reported for FETs fabricated from more established layered metal dichalcogenides, such as MoS_2.

The difference in device quality between back-gated and DI water top-gated FETs is reflected in measurements of the hysteresis under reversal of the gate voltage sweep direction. Except for ultraclean devices (*e.g.*, encapsulated within BN membranes),[62] FETs fabricated from layered metal dichalcogenides typically show significant hysteresis, assigned to charge traps due to surface adsorbates.[63,64] The transfer characteristics of our back gated devices with moderate mobilities (∼2−10 cm^2/(V s)) show significant hysteresis, *i.e.*, are strongly affected by charge trapping (Figure 7 (c)). In contrast, the solution gated devices with much higher carrier mobilities (up to 230 cm^2/(V s)) show only minimal hysteresis (∼15 mV) as the top gate voltage is swept in opposite directions (Figure 7 (d)), *i.e.*, much smaller effects of charge traps at the top and bottom interfaces. This behavior is consistent with the absence of surface adsorbates in the solution environment and an effective screening of interface states at the SnS_2/SiO_2 interface by the high-k dielectric.

Similar to gate-controlled changes in carrier density, light absorption causes an increase in the carrier density and conductance of semiconducting dichalcogenides, allowing them to be used as phototransistors.[15,16] Photoconductivity lends itself as a simple approach to photodetection since only the channel resistance needs to be measured and no p−n junction is required to separate photogenerated electron−hole pairs. Commercially available photoconductive detectors typically incorporate inexpensive cadmium sulfide or lead sulfide as the active material for use in many consumer items such as camera light meters, streetlights, *etc.*, but alternatives avoiding the use of cadmium or lead would be desirable. Metal dichalcogenides, such as SnS_2, have potential for such applications, provided that inexpensive and scalable synthesis methods for the fabrication of high-quality monolayer or few-layer material can be identified.

We demonstrate the implementation of a simple photoresistive element using a back-gated few-layer

SnS_2 FET (with channel thickness ~10 nm; Figure 8 (a)). Figure 8 (b) shows that back gating as well as illumination controls the conductance of the device. Without illumination, a change in back gate voltage from −20 V to 25 V causes a stepwise increase in conductance. Similarly, illumination by a laser diode (532 nm; power at sample ~100 nW) at each of the back-gate voltages raises the conductance by a factor of 2−2.5. The resulting responsivity of ~100 A/W, although lower than the highest values reported for monolayer MoS_2 photodetectors (~10^3 A/W),[16] makes the SnS_2 photo-FET suitable for the detection of low-level DC signals.

Practical photodetectors often require the high-bandwidth detection of pulsed radiation. Previous reports on MoS_2 photodetectors have given conflicting results, either showing slow response times (several seconds)[16] or prompt changes to variations in light intensity on the scale of tens of milliseconds.[15] Our experiments demonstrate that SnS_2 phototransistors allow the detection of intermittent light, and that they share some of the characteristics reported for MoS_2 devices. Figure 8 (c) shows the pulse-response of a typical SnS_2 device, characterized by rise and fall times on the order of seconds and tens of seconds, respectively, independent of back gate voltage and source-drain bias. The long rise and fall times, as well as multiexponential functional forms suggest that long-lived charge traps are responsible for the observed slow response, and that a combination of multiple trap states with different lifetimes produces the observed overall temporal characteristics. The existence of trap states is consistent with the hysteresis in the transfer characteristic of back-gated devices whose channel surface is exposed to ambient air (Figure 7 (c)), and similar behavior observed by ultraviolet photoelectron spectroscopy on bulk SnS_2 crystals with different molecular species intentionally deposited on the surface confirms the key role of adsorbates in generating long-lived charge traps in layered materials.[65] Contributions of short-lived states to the overall signal can be determined by chopping the exciting light at frequencies beyond the cutoff frequency associated with the population of long-lived charge traps. Figure 8 (d) shows measurements, in which the incident light was chopped at a frequency of ~1 Hz. In addition to a constant background due to occupation of states that are too long-lived to follow these changes, evident through the reduced difference between the "on" and "off" (*i.e.*, dark) currents (Figure 8 (d)), there is a smaller component in the photoresponse that shows fast rise times below 50 ms.

It is likely that the fast and slow components of the overall response of our SnS_2 phototransistors are due to a combination of extrinsic traps (*e.g.*, due to adsorbates at the SnS_2 surface and the interface to the underlying SiO_2) as well as defect states in the SnS_2 itself. Future work will aim at identifying the origin of these states, *via* measurements on clean (adsorbate-free) devices in controlled ambient and by varying the concentration of impurities and defects, such as chlorine dopants and sulfur vacancies. Our results suggest that if the origin of the different photoresponse components can be corroborated, metal dichalcogenide phototransistors may be developed for the detection of pulsed light at frequencies in the kHz range, suitable for imaging applications, and possibly down to sub-millisecond response times typical for biased Si photoconductors[66] or picoseconds achieved in III−V photoconductor devices.[67]

CONCLUSIONS

In conclusion, we have used exfoliation from high-quality single crystals combined with comprehensive characterization, device fabrication and measurements on field-effect transistor devices to establish the properties of few-layer and monolayer SnS_2, a layered metal dichalcogenide material whose components are both inexpensive and earth-abundant. We describe several approaches, including optical contrast measurements, atomic-force microscopy, and Raman spectroscopy that are suitable for unambiguously identifying monolayer SnS_2 and for estimating the thickness of few-layer SnS_2. Electronic structure calculations, validated by the first high-quality experimental band dispersion maps on SnS_2, demonstrate distinct differences to other metal dichalcogenides, notably MoS_2. While bulk SnS_2 is a semiconductor with an indirect bandgap of ~2.2 eV, the bandgap remains indirect in few-layer and monolayer flakes, which contrasts with the behavior observed in MoS_2 and is explained by the locations of the valence and conduction band extrema in the Brillouin zone and the contributions to these states primarily from tin s-orbitals and in-plane (x, y) components of the sulfur p-orbitals. Measurements on field-effect devices fabricated from exfoliated few-layer SnS_2 show characteristics that are promising for applications in flexible electronics and photodetection. Whereas ultrathin devices showed high on−off current ratios, the room-temperature field-effect carrier mobility in back-gated few-layer SnS_2/SiO_2 was generally of the order of ~5 $cm^2/(V\ s)$. An increase of the effective mobility with increasing channel thickness suggests that the transport is not limited by scattering at impurities within the chlorine-doped active layer but in the underlying SiO_2 support. This is confirmed by measurements of the field-effect mobility in devices with different channel thickness, and by the characteristics of solution-gated devices that showed enhanced carrier mobilities up to 230 $cm^2/(V\ s)$, as well as negligible hysteresis and near-ideal subthreshold swing in their room temperature transfer characteristics. Finally, we demonstrated light detection in SnS_2 phototransistors. Our results show photoresponse at different time scales, ranging from tens of milliseconds to several

ARTICLE

seconds, similar to the behavior of MoS_2 phototransistors, and suggest that photodetection in metal dichalcogenides such as SnS_2 may be sufficiently fast for imaging applications if avenues can be developed to eliminate the states responsible for the slow photoresponse.

METHODS

The starting materials used in this work were high-quality bulk crystals of layered SnS_2, grown by the vertical Bridgman method, as described previously.[68] The crystals were intentionally chlorine-doped (using $SnCl_4$) to a concentration of 2.3×10^{17} cm^{-3}, and were orange colored (Figure 1 (b)). The layered bulk crystals were easily exfoliated into thinner flakes, including few-layer and monolayer SnS_2. To isolate thin SnS_2, we used mechanical exfoliation using adhesive tape followed by transfer onto a Si wafer covered with 300 nm SiO_2. Prior to the transfer, the substrate was cleaned in an oxygen plasma. Thin (monolayer, bilayer, few-layer) SnS_2 flakes were initially identified by optical microscopy (Nikon, L200N), and then further characterized using other methods.

Atomic force microscopy (Veeco, Multimode V) and confocal Raman spectroscopy/microscopy (WITec alpha 300) were used to measure the properties and thickness of exfoliated SnS_2. A laser wavelength of 532 nm and spot size of $\sim$0.5 μm was used to obtain Raman spectra and spatially resolved Raman maps.

Structural characterization by transmission electron microscopy (TEM) was performed in a FEI Titan 80–300 microscope equipped with a CEOS Cs-corrector. Plan-view TEM samples were prepared by exfoliating SnS_2 flakes from bulk crystals directly onto holey carbon TEM grids. Cross-sectional imaging was performed in areas where the edges of flakes had spontaneously folded over during the exfoliation process.

The crystal structure and electronic properties were investigated in a spectroscopic low-energy electron microscope (SPE-LEEM), situated at beamline U5UA of the National Synchrotron Light Source.[69] A fresh SnS_2 surface was obtained by cleavage in air immediately before inserting the sample into the ultrahigh-vacuum (UHV) load-lock of the LEEM system. Selected-area low-energy electron diffraction (micro-LEED) on small sample areas (2 μm diameter) was used to verify the structure of the crystal. The electronic structure of SnS_2 was mapped at room temperature by collecting angle-resolved photoelectron spectra from micron-sized sample areas (micro-ARPES).[54] Ultraviolet synchrotron radiation with energy $h\nu$ = 42 eV incident perpendicular to the sample was used to excite photoelectrons.

The micro-ARPES band structure measurements were complemented by density-functional theory (DFT) calculations using the projector augmented wave method as implemented in the software package VASP.[70] The screened Heyd–Scuseria–Ernzerhof (HSE) hybrid functional has been employed.[71] A Monkhorst–Pack scheme was adopted to integrate over the Brillouin zone with a k-mesh $9 \times 9 \times 1$ ($8 \times 8 \times 4$) for the monolayer (bulk) SnS_2 structure, and a plane-wave basis kinetic energy cutoff of 300 eV was used. To determine the electronic band structure of bulk SnS_2 we used the 4H-SnS_2 structure, consistent with the polytype identified in our experiments. The lattice constant of monolayer SnS_2 was obtained from the DFT-D2 volume optimized bulk SnS_2 structure,[72] and the atomic coordinates for the monolayer were optimized at this fixed lattice constant. To simulate the monolayer, a vacuum spacing of 15 Å was used. For the HSE calculations, 25% short-range exact Hartree–Fock exchange was used with the Perdew–Burke–Ernzerhof (PBE) correlation. The HSE screening parameter, μ, was empirically set to 0.3 (1/Å) for both the bulk and monolayer. Projected density of states calculations were performed by integrating over the Brillouin zone using the tetrahedron method with Blöchl corrections.[73]

The electrical transport properties of thin (monolayer, few-layer) SnS_2 were determined using microfabricated field-effect transistors (FETs). After exfoliating SnS_2 flakes onto 300 nm SiO_2/Si, we fabricated test devices using standard optical lithography and deposited Ti/Au (5 nm/50 nm) as contact electrodes using electron-beam evaporation. The final devices were annealed in high vacuum (10^{-8} Torr) at 300 °C for 10 h in order to remove resist residues and enhance the metallic contacts. While most of the FETs used back-gating *via* the SiO_2/Si substrate, we also fabricated several devices that were top-gated using deionized (DI) water as the dielectric. In these devices, PMMA was spin-coated on the entire chip, and windows over the FET channel were defined by electron-beam lithography. To test the contacts, current–voltage characteristics were first measured for different carrier densities, tuned by back-gating before introducing DI water as top gate. DI water was dropped in the center of the device, ensuring that the metal electrodes were not contacted by water.

Measurements on SnS_2 phototransistors were carried out at room temperature on two probe stations, one in ambient air and the other in UHV. The devices were well-characterized FETs, fabricated as discussed above. A halogen lamp and a green laser (λ = 532 nm, 1 mW) were used as light sources. The optical power on the device was estimated from the output power of the laser and the fraction of the (unfocused) beam illuminating the active area of the phototransistor. Measurements with pulsed light used a mechanical chopper at variable frequency.

Conflict of Interest: The authors declare no competing financial interest.

Acknowledgment. Research carried out at the Center for Functional Nanomaterials and National Synchrotron Light Source, Brookhaven National Laboratory, which is supported by the U.S. Department of Energy, Office of Basic Energy Sciences, under Contract No. DE-AC02-98CH10886. OLAM and DAR gratefully acknowledge support under National Science Foundation Grant No. CHE-1213243. MRN, DW, and RKL acknowledge support from the National Science Foundation Grants No. 1124733 and 1128304 and FAME, one of six centers of STARnet, a Semiconductor Research Corporation program sponsored by MARCO and DARPA. This work used the Extreme Science and Engineering Discovery Environment (XSEDE), which is supported by NSF Grant No. OCI-1053575, and Information Technology at Purdue University, West Lafayette, IN, USA.

Supporting Information Available: Supplementary methods. Supplementary experimental results and figures: Optical absorption measurements; microphotoluminescence spectroscopy; plasma etching of SnS_2; analysis of the field-effect mobility of solution gated SnS_2 transistors. Supplementary references. This material is available free of charge *via* the Internet at http://pubs.acs.org.

REFERENCES AND NOTES

1. Novoselov, K. S.; Jiang, D.; Schedin, F.; Booth, T. J.; Khotkevich, V. V.; Morozov, S. V.; Geim, A. K. Two-Dimensional Atomic Crystals. *Proc. Natl. Acad. Sci. U. S. A.* **2005**, *102*, 10451–10453.
2. Novoselov, K. S.; Geim, A. K.; Morozov, S. V.; Jiang, D.; Katsnelson, M. I.; Grigorieva, I. V.; Dubonos, S. V.; Firsov, A. A. Two-Dimensional Gas of Massless Dirac Fermions in Graphene. *Nature* **2005**, *438*, 197–200.
3. Novoselov, K. S.; Geim, A. K.; Morozov, S. V.; Jiang, D.; Zhang, Y.; Dubonos, S. V.; Grigorieva, I. V.; Firsov, A. A. Electric Field Effect in Atomically Thin Carbon Films. *Science* **2004**, *306*, 666–669.
4. Zhang, Y.; Tan, J. W.; Stormer, H. L.; Kim, P. Experimental Observation of the Quantum Hall Effect and Berry's Phase in Graphene. *Nature* **2005**, *438*, 201–204.
5. Habib, K. M. M.; Sylvia, S. S.; Ge, S.; Neupane, M.; Lake, R. K. The Coherent Interlayer Resistance of a Single, Rotated Interface between Two Stacks of AB Graphite. *Appl. Phys. Lett.* **2013**, *103*, 243114.

6. Lee, C.; Wei, X.; Kysar, J. W.; Hone, J. Measurement of the Elastic Properties and Intrinsic Strength of Monolayer Graphene. *Science* **2008**, *321*, 385–388.
7. Nair, R. R.; Blake, P.; Grigorenko, A. N.; Novoselov, K. S.; Booth, T. J.; Stauber, T.; Peres, N. M. R.; Geim, A. K. Fine Structure Constant Defines Visual Transparency of Graphene. *Science* **2008**, *320*, 1308.
8. Schedin, F.; Geim, A. K.; Morozov, S. V.; Hill, E. W.; Blake, P.; Katsnelson, M. I.; Novoselov, K. S. Detection of Individual Gas Molecules Adsorbed on Graphene. *Nat. Mater.* **2007**, *6*, 652–655.
9. Levendorf, M. P.; Kim, C.-J.; Brown, L.; Huang, P. Y.; Havener, R. W.; Muller, D. A.; Park, J. Graphene and Boron Nitride Lateral Heterostructures for Atomically Thin Circuitry. *Nature* **2012**, *488*, 627–632.
10. Liu, Z.; Ma, L.; Shi, G.; Zhou, W.; Gong, Y.; Lei, S.; Yang, X.; Zhang, J.; Yu, J.; Hackenberg, K. P.; *et al.* In-Plane Heterostructures of Graphene and Hexagonal Boron Nitride with Controlled Domain Sizes. *Nat. Nanotechnol.* **2013**, *8*, 119–124.
11. Sutter, P.; Cortes, R.; Lahiri, J.; Sutter, E. Interface Formation in Monolayer Graphene-Boron Nitride Heterostructures. *Nano Lett.* **2012**, *12*, 4869–4874.
12. Britnell, L.; Gorbachev, R. V.; Jalil, R.; Belle, B. D.; Schedin, F.; Mishchenko, A.; Georgiou, T.; Katsnelson, M. I.; Eaves, L.; Morozov, S. V.; *et al.* Field-Effect Tunneling Transistor Based on Vertical Graphene Heterostructures. *Science* **2012**, *335*, 947–950.
13. Wang, Q. H.; Kalantar-Zadeh, K.; Kis, A.; Coleman, J. N.; Strano, M. S. Electronics and Optoelectronics of Two-Dimensional Transition Metal Dichalcogenides. *Nat. Nanotechnol.* **2012**, *7*, 699–712.
14. Radisavljevic, B.; Radenovic, A.; Brivio, J.; Giacometti, V.; Kis, A. Single-Layer MoS_2 Transistors. *Nat. Nanotechnol.* **2011**, *6*, 147–150.
15. Yin, Z.; Li, H.; Li, H.; Jiang, L.; Shi, Y.; Sun, Y.; Lu, G.; Zhang, Q.; Chen, X.; Zhang, H. Single-Layer MoS_2 Phototransistors. *ACS Nano* **2012**, *6*, 74–80.
16. Lopez-Sanchez, O.; Lembke, D.; Kayci, M.; Radenovic, A.; Kis, A. Ultrasensitive Photodetectors Based on Monolayer MoS_2. *Nat. Nanotechnol.* **2013**, *8*, 497–501.
17. Britnell, L.; Ribeiro, R. M.; Eckmann, A.; Jalil, R.; Belle, B. D.; Mishchenko, A.; Kim, Y.-J.; Gorbachev, R. V.; Georgiou, T.; Morozov, S. V.; *et al.* Strong Light-Matter Interactions in Heterostructures of Atomically Thin Films. *Science* **2013**, *340*, 1311–1314.
18. Bernardi, M.; Palummo, M.; Grossman, J. C. Extraordinary Sunlight Absorption and One Nanometer Thick Photovoltaics Using Two-Dimensional Monolayer Materials. *Nano Lett.* **2013**, *13*, 3664–3670.
19. Splendiani, A.; Sun, L.; Zhang, Y.; Li, T.; Kim, J.; Chim, C.-Y.; Galli, G.; Wang, F. Emerging Photoluminescence in Monolayer MoS_2. *Nano Lett.* **2010**, *10*, 1271–1275.
20. Mak, K. F.; Lee, C.; Hone, J.; Shan, J.; Heinz, T. F. Atomically Thin MoS_2: A New Direct-Gap Semiconductor. *Phys. Rev. Lett.* **2010**, *105*, 136805.
21. Jin, W.; Yeh, P.-C.; Zaki, N.; Zhang, D.; Sadowski, J. T.; Al-Mahboob, A.; van der Zande, A. M.; Chenet, D. A.; Dadap, J. I.; Herman, I. P.; *et al.* Direct Measurement of the Thickness-Dependent Electronic Band Structure of MoS_2 Using Angle-Resolved Photoemission Spectroscopy. *Phys. Rev. Lett.* **2013**, *111*, 106801.
22. Wickramaratne, D.; Zahid, F.; Lake, R. K. Electronic and Thermoelectric Properties of Few-Layer Transition Metal Dichalcogenides. *J. Chem. Phys.* **2014**, 140.
23. Xiao, D.; Liu, G.-B.; Feng, W.; Xu, X.; Yao, W. Coupled Spin and Valley Physics in Monolayers of MoS_2 and Other Group-Vi Dichalcogenides. *Phys. Rev. Lett.* **2012**, *108*, 196802.
24. Mak, K. F.; He, K.; Shan, J.; Heinz, T. F. Control of Valley Polarization in Monolayer MoS_2 by Optical Helicity. *Nat. Nanotechnol.* **2012**, *7*, 494–498.
25. Van der Zande, A. M.; Huang, P. Y.; Chenet, D. A.; Berkelbach, T. C.; You, Y.; Lee, G.-H.; Heinz, T. F.; Reichman, D. R.; Muller, D. A.; Hone, J. C. Grains and Grain Boundaries in Highly Crystalline Monolayer Molybdenum Disulphide. *Nat. Mater.* **2013**, *12*, 554–561.
26. Parkinson, B. A. Dye Sensitization of Van Der Waals Surfaces of Tin Disulfide Photoanodes. *Langmuir* **1988**, *4*, 967–976.
27. Fotouhi, B.; Katty, A.; Gorochov, O. Photoelectrochemical and Corrosion Study of N-Type SnSSe. *J. Electrochem. Soc.* **1985**, *132*, 2181–2184.
28. Schlaf, R.; Louder, D.; Lang, O.; Pettenkofer, C.; Jaegermann, W.; Nebesny, K. W.; Lee, P. A.; Parkinson, B. A.; Armstrong, N. R. Molecular Beam Epitaxy Growth of Thin Films of SnS_2 and $SnSe_2$ on Cleaved Mica and the Basal Planes of Single-Crystal Layered Semiconductors: Reflection High-Energy Electron Diffraction, Low-Energy Electron Diffraction, Photoemission, and Scanning Tunneling Microscopy/Atomic Force Microscopy Characterization. *J. Vac. Sci. Technol., A* **1995**, *13*, 1761–1767.
29. Parkinson, B. Layer-by-Layer Nanometer Scale Etching of Two-Dimensional Substrates Using the Scanning Tunneling Microscope. *J. Am. Chem. Soc.* **1990**, *112*, 7498–7502.
30. Delawski, E.; Parkinson, B. A. Layer-by-Layer Etching of Two-Dimensional Metal Chalcogenides with the Atomic Force Microscope. *J. Am. Chem. Soc.* **1992**, *114*, 1661–1667.
31. Sun, Y.; Cheng, H.; Gao, S.; Sun, Z.; Liu, Q.; Liu, Q.; Lei, F.; Yao, T.; He, J.; Wei, S.; *et al.* Freestanding Tin Disulfide Single-Layers Realizing Efficient Visible-Light Water Splitting. *Angew. Chem., Int. Ed.* **2012**, *51*, 8727–8731.
32. Debtanu, D.; John, M.; Sean, S.; Vincent, Z.; Arnold, G.; Haibing, P. High On/Off Ratio Field Effect Transistors Based on Exfoliated Crystalline SnS_2 Nano-Membranes. *Nanotechnology* **2013**, *24*, 025202.
33. Pan, T. S.; De, D.; Manongdo, J.; Guloy, A. M.; Hadjiev, V. G.; Lin, Y.; Peng, H. B. Field Effect Transistors with Layered Two-Dimensional $SnS_{2-x}Se_x$ Conduction Channels: Effects of Selenium Substitution. *Appl. Phys. Lett.* **2013**, *103*, 093108.
34. Song, H. S.; Li, S. L.; Gao, L.; Xu, Y.; Ueno, K.; Tang, J.; Cheng, Y. B.; Tsukagoshi, K. High-Performance Top-Gated Monolayer SnS_2 Field-Effect Transistors and Their Integrated Logic Circuits. *Nanoscale* **2013**, *5*, 9666–9670.
35. Mitchell, R. S.; Fujiki, Y.; Ishizawa, Y. Structural Polytypism of SnS_2. *Nature* **1974**, *247*, 537–538.
36. Palosz, B.; Palosz, W.; Gierlotka, S. Structures of 24 New Polytypes of Tin Disulphide. *Acta Crystallogr., Sect. C: Cryst. Struct. Commun.* **1985**, *41*, 1402–1404.
37. Mitchell, R. S.; Fujiki, Y.; Ishizawa, Y. Structural Polytypism of Tin Disulfide: Its Relationship to Environments of Formation. *J. Cryst. Growth* **1982**, *57*, 273–279.
38. Palosz, B.; Steurer, W.; Schulz, H. Refinement of SnS_2 Polytypes 2H, 4H and 18R. *Acta Crystallogr. Sec. B* **1990**, *46*, 449–455.
39. Roddaro, S.; Pingue, P.; Piazza, V.; Pellegrini, V.; Beltram, F. The Optical Visibility of Graphene: Interference Colors of Ultrathin Graphite on SiO_2. *Nano Lett.* **2007**, *7*, 2707–2710.
40. Gorbachev, R. V.; Riaz, I.; Nair, R. R.; Jalil, R.; Britnell, L.; Belle, B. D.; Hill, E. W.; Novoselov, K. S.; Watanabe, K.; Taniguchi, T.; *et al.* Hunting for Monolayer Boron Nitride: Optical and Raman Signatures. *Small* **2011**, *7*, 465–468.
41. Benameur, M. M.; Radisavljevic, B.; Héron, J. S.; Sahoo, S.; Berger, H.; Kis, A. Visibility of Dichalcogenide Nanolayers. *Nanotechnology* **2011**, *22*, 125706.
42. Li, H.; Lu, G.; Yin, Z.; He, Q.; Li, H.; Zhang, Q.; Zhang, H. Optical Identification of Single- and Few-Layer MoS_2 Sheets. *Small* **2012**, *8*, 682–686.
43. Lee, C.; Yan, H.; Brus, L. E.; Heinz, T. F.; Hone, J.; Ryu, S. Anomalous Lattice Vibrations of Single- and Few-Layer MoS_2. *ACS Nano* **2010**, *4*, 2695–2700.
44. Ferrari, A. C.; Meyer, J. C.; Scardaci, V.; Casiraghi, C.; Lazzeri, M.; Mauri, F.; Piscanec, S.; Jiang, D.; Novoselov, K. S.; Roth, S.; *et al.* Raman Spectrum of Graphene and Graphene Layers. *Phys. Rev. Lett.* **2006**, *97*, 187401–4.
45. Smith, A. J.; Meek, P. E.; Liang, W. Y. Raman Scattering Studies of SnS_2 and $SnSe_2$. *J. Phys. C* **1977**, *10*, 1321.
46. Stadelmann, P. A. *Jems-Ems* Java Version. http://cimewww.epfl.ch/people/stadelmann/jemsWebSite/jems.html.
47. Fong, C. Y.; Cohen, M. L. Electronic Energy-Band Structure of SnS_2 and $SnSe_2$. *Phys. Rev. B: Solid State* **1972**, *5*, 3095–3101.

48. Powell, M. J.; Marseglia, E. A.; Liang, W. Y. The Effect of Polytypism on the Band Structure of SnS_2. *J. Phys. C* **1978**, *11*, 895–904.
49. Robertson, J. Electronic Structure of SnS_2, $SnSe_2$, CdI_2 and PbI_2. *J. Phys. C* **1979**, *12*, 4753–4766.
50. He, X.; Shen, H. *Ab Initio* Calculations of Band Structure and Thermophysical Properties for SnS_2 and $SnSe_2$. *Phys. B* **2012**, *407*, 1146–1152.
51. Seminovski, Y.; Palacios, P.; Wahnon, P. Effect of Van Der Waals Interaction on the Properties of SnS_2 Layered Semiconductor. *Thin Solid Films* **2013**, *535*, 387–389.
52. Margaritondo, G.; Rowe, J. E. Synchrotron-Radiation Photoemission Spectroscopy of Octahedrally Coordinated Layer Compounds. *Phys. Rev. B: Condens. Matter Mater. Phys.* **1979**, *19*, 3266–3275.
53. Bertrand, Y.; Barski, A.; Pincheaux, R. Experimental Valence-Band Structure of Tin Disulfide SnS_2. *Phys. Rev. B: Condens. Matter Mater. Phys.* **1985**, *31*, 5494–5496.
54. Sutter, P.; Hybertsen, M. S.; Sadowski, J. T.; Sutter, E. Electronic Structure of Few-Layer Epitaxial Graphene on Ru(0001). *Nano Lett.* **2009**, *9*, 2654–2660.
55. Podzorov, V.; Gershenson, M. E.; Kloc, C.; Zeis, R.; Bucher, E. High-Mobility Field-Effect Transistors Based on Transition Metal Dichalcogenides. *Appl. Phys. Lett.* **2004**, *84*, 3301–3303.
56. Farmer, D. B.; Lin, Y.-M.; Avouris, P. Graphene Field-Effect Transistors with Self-Aligned Gates. *Appl. Phys. Lett.* **2010**, *97*, 013103.
57. Kosuke, N.; Tomonori, N.; Koji, K.; Akira, T. Mobility Variations in Mono- and Multi-Layer Graphene Films. *Appl. Phys. Express* **2009**, *2*, 025003.
58. Pu, J.; Zhang, Y.; Wada, Y.; Tse-Wei Wang, J.; Li, L.-J.; Iwasa, Y.; Takenobu, T. Fabrication of Stretchable MoS_2 Thin-Film Transistors Using Elastic Ion-Gel Gate Dielectrics. *Appl. Phys. Lett.* **2013**, *103*, 023505.
59. Hess, L. H.; Seifert, M.; Garrido, J. A. Graphene Transistors for Bioelectronics. *Proc. IEEE* **2013**, *101*, 1780–1792.
60. Ye, J. T.; Zhang, Y. J.; Akashi, R.; Bahramy, M. S.; Arita, R.; Iwasa, Y. Superconducting Dome in a Gate-Tuned Band Insulator. *Science* **2012**, *338*, 1193–1196.
61. Bollinger, A. T.; Dubuis, G.; Yoon, J.; Pavuna, D.; Misewich, J.; Bozovic, I. Superconductor-Insulator Transition in $La_{2-x}Sr_xCuO_4$ at the Pair Quantum Resistance. *Nature* **2011**, *472*, 458–460.
62. Lee, G.-H.; Yu, Y.-J.; Cui, X.; Petrone, N.; Lee, C.-H.; Choi, M. S.; Lee, D.-Y.; Lee, C.; Yoo, W. J.; Watanabe, K.; *et al.* Flexible and Transparent MoS_2 Field-Effect Transistors on Hexagonal Boron Nitride-Graphene Heterostructures. *ACS Nano* **2013**, *7*, 7931–7936.
63. Late, D. J.; Liu, B.; Matte, H. S. S. R.; Dravid, V. P.; Rao, C. N. R. Hysteresis in Single-Layer MoS_2 Field Effect Transistors. *ACS Nano* **2012**, *6*, 5635–5641.
64. Choi, M. S.; Lee, G.-H.; Yu, Y.-J.; Lee, D.-Y.; Hwan Lee, S.; Kim, P.; Hone, J.; Jong Yoo, W. Controlled Charge Trapping by Molybdenum Disulphide and Graphene in Ultrathin Heterostructured Memory Devices. *Nat. Commun.* **2013**, *4*, 1624.
65. Racke, D.; Monti, O. L. A. Persistent Non-Equilibrium Interface Dipoles at Quasi-2D Organic/Inorganic Semiconductor Interfaces: The Effect of Gap States. *Surf. Sci.* **2014**, *630*, 136–143.
66. Li, X.; Carey, J. E.; Sickler, J. W.; Pralle, M. U.; Palsule, C.; Vineis, C. J. Silicon Photodiodes with High Photoconductive Gain at Room Temperature. *Opt. Express* **2012**, *20*, 5518–5523.
67. Anderson, G. W.; Papanicolaou, N. A.; Thompson, P. E.; Boos, J. B.; Carruthers, T. F.; Ma, D. I.; Mack, I. A. G.; Modolo, J. A.; Kub, F. J. High-Speed Planar GaAs Photoconductors with Surface Implant Layers. *Appl. Phys. Lett.* **1988**, *53*, 313–315.
68. Sharp, L.; Soltz, D.; Parkinson, B. A. Growth and Characterization of Tin Disulfide Single Crystals. *Cryst. Growth Des.* **2006**, *6*, 1523–1527.
69. Flege, J. I.; Vescovo, E.; Nintzel, G.; Lewis, L. H.; Hulbert, S.; Sutter, P. A New Soft X-Ray Photoemission Microscopy Beamline at the National Synchrotron Light Source. *Nucl. Instrum. Methods Phys. Res., Sect. B* **2007**, *261*, 855–858.
70. Kresse, G.; Furthmüller, J. Efficient Iterative Schemes for *Ab Initio* Total-Energy Calculations Using a Plane-Wave Basis Set. *Phys. Rev. B: Condens. Matter Mater. Phys.* **1996**, *54*, 11169–11186.
71. Heyd, J.; Scuseria, G. E.; Ernzerhof, M. Hybrid Functionals Based on a Screened Coulomb Potential. *J. Chem. Phys.* **2003**, *118*, 8207–8215.
72. Grimme, S. Semiempirical GGA-Type Density Functional Constructed with a Long-Range Dispersion Correction. *J. Comput. Chem.* **2006**, *27*, 1787–1799.
73. Blöchl, P. E.; Jepsen, O.; Andersen, O. K. Improved Tetrahedron Method for Brillouin-Zone Integrations. *Phys. Rev. B: Condens. Matter Mater. Phys.* **1994**, *49*, 16223–16233.